Journal of Power Sources 196 (2011) 5526–5537

Contents lists available at ScienceDirect

Journal of Power Sources

journal homepage: www.elsevier.com/locate/jpowsour

Experimental characterization and mechanistic modeling of carbon monoxide fueled solid oxide fuel cell

Yixiang Shi*, Chen Li, Ningsheng Cai

Key Laboratory for Thermal Science and Power Engineering of Ministry of Education, Tsinghua University, Beijing 100084, China

ARTICLE INFO

Article history:
Received 22 November 2010
Received in revised form 4 February 2011
Accepted 4 February 2011
Available online 12 February 2011

Keywords:
Solid oxide fuel cell
Elementary reaction
Heterogeneous chemistry
Electrochemistry
Anode

ABSTRACT

The paper presents an elementary reaction based solid oxide fuel cell (SOFC) model coupled with anodic elementary heterogeneous reactions and electrochemical charge transfer reactions for CO/CO_2 fuel based on an anode supported button cell. The model is calibrated and validated using experimental data obtained for various CO/CO_2 fuel compositions at 750, 800 and 850 °C. The comparison shows that the modeling results agree well with the experimental data. The effects of operating conditions on the cell performance and the detailed species concentration distribution are predicted. Then, the carbon deposition on the SOFC anode with CO/CO_2 fuel is experimentally measured and simulated using the elementary reaction model. The results indicate that lower temperature and lower operation voltage are helpful to reduce the possibilities of carbon deposition on Ni particle surfaces.

1. Introduction

Solid oxide fuel cells (SOFCs) are known for their fuel flexibility and tolerance to carbon monoxide, CO, besides their high efficiency, low environmental impacts and system simplicity for stationary or mobile applications. Syngas, a mixture of carbon monoxide, CO, and hydrogen, H_2, derived from steam reforming of coal, biomass, methane, or other hydrocarbons, can be used in an SOFC directly in generating electricity.

In order to optimize the anode performance, it is important to investigate the comprehensive electrochemical oxidation processes within SOFC anode integrating with experimental data and kinetic mechanisms. Since it is difficult to clarify internal parameter distribution and complex physical phenomenon in fuel cell only by the expensive, time-consuming and labor-intensive experiments, a validated mechanistic model will be an effective method for internal phenomenon predictions, performance evaluation and optimal design of the SOFCs.

With respect to performance, it is generally agreed that the electrochemical reaction rate of CO is lower than that of H_2 [1–3]. When pure CO is supplied to a porous anode, Jiang and Virkar [4] reported that the maximum power density is about 40% of that obtained using pure H_2. The wide variety of experimental conditions and materials in CO electrochemical oxidation result in different reaction mechanisms and different limiting steps being proposed by different researchers [5,6], and related mechanistic model has been developed [7,8]. However, it should be noted that compared with the systematic experimental and theoretical studies of H_2 electrochemical oxidation [9–17], relative fewer studies have been performed for the CO electrochemical oxidation mechanism, especially for the elementary reaction level models of SOFC with CO/CO_2 fuel.

In this paper, an elementary reaction based SOFC model coupled with anodic elementary heterogeneous reactions and electrochemical elementary charge transfer reactions for CO/CO_2 fuel is developed based on an anode support button cell. The developed model is calibrated and validated using experimental data obtained on a button cell for various CO/CO_2 fuel compositions at 750, 800 and 850 °C. Then, the effects of operating conditions on the cell performance and the detailed species concentration distribution are predicted. Finally, the carbon deposition in the SOFC anode with CO/CO_2 fuel is experimentally measured and simulated using the elementary reaction model.

2. Experiment

2.1. Anode-supported button cell structure and fabrication

An anode-supported SOFC button cell made by SICCAS (Shanghai Institute of Ceramics Chinese Academy of Sciences) was employed in this study. It consisted of a Ni/YSZ anode support layer (680 μm), a Ni/ScSZ anode active interlayer (15 μm), a ScSZ electrolyte layer (20 μm), and a lanthanum strontium manganate (LSM)/ScSZ cathode layer (15 μm). The diameter of cathode layer

* Corresponding author. Tel.: +86 10 62789955; fax: +86 10 62770209.
E-mail address: shyx@tsinghua.edu.cn (Y. Shi).

0378-7753/$ – see front matter © 2011 Elsevier B.V. All rights reserved.
doi:10.1016/j.jpowsour.2011.02.013

Nomenclature

a_i	pre-exponential factor in sticking coefficient expression
A	pre-exponential factor (cm, mol, s)
b_i	temperature exponent in sticking coefficient expression
c	concentration ($mol\,m^{-3}$)
d_i	activation energy in sticking coefficient expression ($J\,mol^{-1}$)
D	diffusion coefficient ($m^2\,s^{-1}$)
E	activation energy ($J\,mol^{-1}$)
E_{ca}	parameter in Eq. (23) ($130{,}000\,J\,mol^{-1}$)
F	Faraday constant ($96{,}485\,C\,mol^{-1}$)
i_0	exchange current density ($A\,m^{-2}$)
$i_{0,an}$	anodic length specific current density ($A\,m^{-1}$)
I_F	volumetric Faradaic current ($A\,m^{-3}$)
k	reaction rate constant (m, mol, s)
K	number of species
M_k, M_j	molecular weight ($kg\,mol^{-1}$)
n	temperature exponent
n_e	number of electrons participating in the reaction
n_t	total number of particles per unit volume
N	number of the reactions
p	pressure (Pa)
P	whole range connection probabilities of same kind particles
Q	source term of charge balance equations ($A\,m^{-3}$)
$\bar{r}$	average pore size (m)
r_{el}	mean radius of the electronic conductor particle (m)
R	gas constant ($8.314\,J\,mol^{-1}\,K^{-1}$)
R_k	source term of mass balance equations ($kg\,m^{-3}\,s^{-1}$)
$\dot{s}$	molar production rate ($mol\,m^{-2}\,s^{-1}$)
S^0	initial sticking coefficient
S^{eff}	effective reaction area per unit volume ($m^2\,m^{-3}$)
S_{Ni}	Ni active surface area per unit volume ($m^2\,m^{-3}$)
S_{TPB}	TPB active area per unit volume ($m^2\,m^{-3}$)
t	time (s)
T	temperature (K)
V	voltage (V)
V_k, V_j	diffusion volume
W	molecular weight of the gas-phase species in sticking coefficient reaction ($kg\,mol^{-1}$)
x_k	molar fraction of gas-phase species k
Z	coordination number

Greek letters

α	transfer coefficient
β	tuning parameter ($\Omega^{-1}\,m^{-2}$)
γ	parameter modeling the rate constant from sticking coefficient
Γ	surface sites density ($mol\,m^{-2}$)
ε	porosity
ε_{ki}	parameter modeling the species coerage
η	overpotential (V)
θ	contact angle between the electronic and ionic conductors particles (rad)
θ_k	surface coverage of species k
μ_{ki}	parameter modeling the species coverage
ν	stoichiometric coefficient
σ	conductivity ($S\,m^{-1}$)
τ	tortuosity
χ	species symbol

Subscripts

ac	anode chamber
act	active layer
an	anode
ca	cathode
cc	cathode chamber
ec	electrochemical reactions
el	electronic conductor particles
elec	electronic
electrolyte	electrolyte
g	gas-phase species
i	reactions index
io	ionic conductor particles
ion	ionic
k	species index
Kn	Knudsen
mole	molecular
OCV	open circuit voltage
ref	reference
s	surface species
sp	support layer

Superscripts

0	parameter at equilibrium conditions
bulk	bulk phase
eff	effective
TPB	three phase boundary

was 1.3 cm and diameters of other layers were all 2.6 cm. Before testing, silver paste was reticulated on the anode and cathode surface by screen-printing for current collection.

2.2. Test setup

The experimental setup can be shown in Fig. 1(a). The button cell was located at the end of two coaxial alumina tubes and was impacted by an alumina plate which was strained by springs. The Pt mesh was used as the cathode current collector and was fixed to the porous cathode with silver paste screen-printed on the surface. The oxidant flowed into the inner tube to the cathode and passed through the porous Pt mesh. A Ni felt (thickness 2 mm) was fixed to the anode support layer with silver paste to collect anode current. The fuel was induced to the anode surrounding by an alumina tube. Due to the porous structure of Pt mesh, the anode gas reached the anode easily. For both anode and cathode, Pt wires were used as voltage and current probes. A glass ring was used as sealant to separate the anode gas and cathode gas. All the devices were enclosed in one quartz tube and heated by a furnace to keep the operation temperature. Pure H_2 was sent to the chamber for 1 h to fully reduce the anode at the flow rate of 50 sccm. Then, CO/CO_2 mixtures with different composition proportions were used as fuel.

2.3. Cell performance tests

The button cell performances were measured experimentally at three temperatures (750/800/850 °C) with different ratios of CO and CO_2, as listed in Table 1. Oxygen was used as oxidant. The flow rates of fuel and oxidant were both kept at 300 sccm.

The polarization curves were measured using four-probe method with an electrochemical workstation (IM6ex, Zahner-Elektrik GmbH, Germany). Electrochemical impedance spectroscopy (EIS) was performed using amplitude of 10 mV over the frequency from 0.1 Hz to 100 kHz. The ohmic resistance of but-

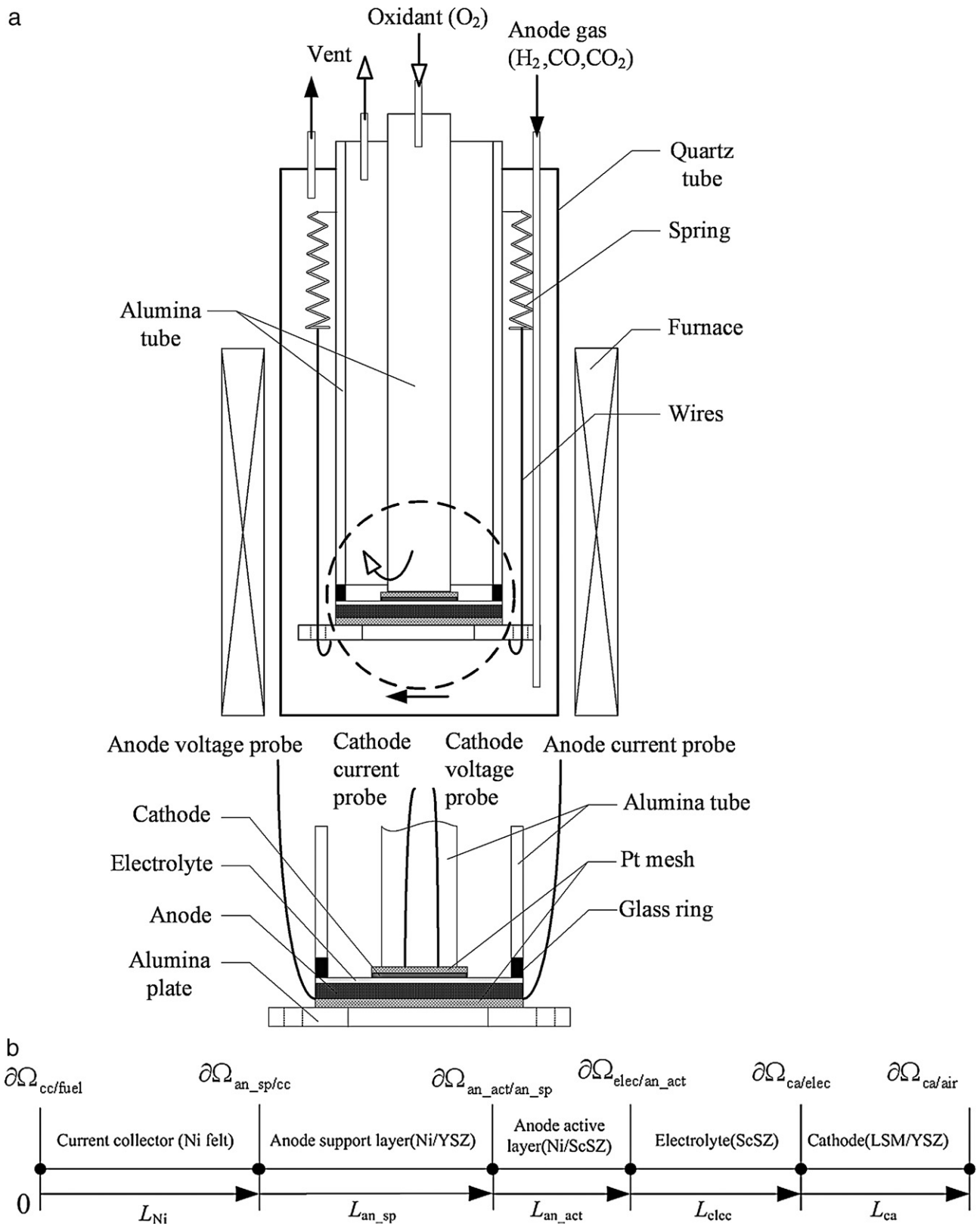

Fig. 1. Illustration of the (a) experimental setup and (b) 1D model geometry of SOFC button cell.

ton cell was estimated from the high frequency intercept of the impedance curve. The measurements were initiated when the temperature changes 30 min later until the system was stable. After the cell tests, the microstructure of anode was characterized using mercury porosimeter.

2.4. Experimental characterization for surface carbon deposition

In order to study the effects of temperature on the anodic carbon depositions, a mixture of CO/CO_2 with 90% CO and 10% CO_2 was used as fuel and the cell was kept discharging at 0.7 V,

Table 1
Gas composition of the fuel in the experimental measurements.

Temperature (°C)	Fuel type	Fuel composition	
		CO (%)	CO_2 (%)
750	F750-1	80	10
	F750-2	40	20
	F750-3	20	40
	F750-4	10	80
800	F800-1	80	10
	F800-2	40	20
	F800-3	20	40
	F800-4	10	80
850	F850-1	80	10
	F850-2	40	20
	F850-3	20	40
	F850-4	10	80

750/800/850 °C, for 2 h after the cell anode is fully reduced as shown in Table 2. Then, in order to study the effects of fuel compositions on the anodic carbon depositions, fuel with different CO/CO_2 ratios was used as fuel and the cell was kept discharging at 0.7 V, 750 °C, for 8 h after the cell anode is fully reduced. It should be noted that, since the long time operation at higher temperature will have effects on cell structures which deteriorate the cell performance. Thus, we choose 2 h discharging time for the experiments set I and 8 h discharging time for the experiments set II.

After the carbon deposition operation, the cell was cooled down to ambient with Ar (150 ml min^{-1}) and H_2 (3 ml min^{-1}) used as protecting gas. About 2% H_2 was added to maintain a reducing atmosphere in the anode chamber to prevent oxidization of the deposited carbon within the anode.

The surfaces of the anode cross-sections were analyzed by a X-ray photoelectron spectroscopy (XPS) (PHI Quantera, ULVAC-PHI, Kanagawa, Japan) with a monochromatic Al Kα ($h\nu$ = 1486.7 eV) X-ray source. To avoid any influence of carbon contamination during the sample transfer and handing, all the sample surfaces were peeled 1.2 nm by an electron gun before characterization. The spot size for analysis was 300 μm × 300 μm. To compensate for the surface-charge effects, the binding energy scale was calibrated with reference to the binding energy of O 1s at 530.2 eV. The survey scans were acquired between 1200 and 0 eV. The elemental surface composition was calculated using the transmission values with relative sensitivity factors specific for the instrument equipped with an Al source.

3. Model development

3.1. Model assumptions and geometry

The following model assumptions were shown as follows:

Table 2
Control experiments for the anode carbon deposition.

Experiments	Operating conditions			
	Temperature	Fuel compositon	Discharging voltage	Discharging time
Set I	750/800/850 °C	90% CO, 10% CO_2	0.7 V	2 *h*
Set II	750 °C	90% CO, 10% CO_2 50% CO, 50% CO_2 10% CO, 90% CO_2	0.7 V	8 h

(1) Gases are assumed as ideal gases.
(2) The temperature of the cell is uniform. All parameters are evaluated at the given temperature.
(3) The electrochemical mechanism is modeled using a set of elementary reactions that represent chemical reactivity at the molecular scale. Heterogeneous thermochemical and electrochemical reactions are assumed to take place on both of the Ni surface and YSZ surface. One adsorbed CO molecule occupies one vacant position on the surface, neglecting the possibility of two vacant positions being
(4) The charge transfer reaction is assumed to be a oxygen spillover reaction taking place at the TPB as: $CO(Ni) + O^{2-}(YSZ) \rightleftarrows CO_2(Ni) + (YSZ) + 2e^-$
(5) The microstructures of electrodes are stable and homogeneous in operation. The carbon deposition influence to the pore structure and reaction activities in anode is disregarded. Besides, the distributions of the two conducting phases (electronic and ionic) in electrodes are assumed to be uniform.
(6) For anode heterogeneous reactions, mean field approximation is used, i.e. the surface adsorbates are assumed to be uniformly distributed over the catalyst surface. And the transport of surface species over microscopic distances caused by surface diffusion is assumed to be negligible.

One-dimensional (1D) geometry is used as illustrated in Fig. 1(b). The model calculation domains and boundaries are labeled schematically in the figure. With the above assumptions and simplified model geometry, a 1D SOFC model is developed by considering anodic heterogeneous chemistry, charge transfer processes, charge balance as well as mass balance.

3.2. Governing equations

3.2.1. Anode heterogeneous chemistry

Heterogeneous chemistry at the catalytic surface of the anode is used. Ni is an effective catalyst for surface reactions, especially for hydrocarbon fueled SOFC. A heterogeneous mechanism simplified from the works of Hecht et al. [18], Janardhanan and Deutschmann [19] and Zhu and Kee [20] is used, as shown in Table 3.

The surface adsorbates are assumed to be uniformly distributed over the Ni surface. The species molar production rates depend on the gaseous species concentrations and the surface species concentrations, which are expressed by the coverage. The coverage θ_k is the fraction of the surface sites covered by the adsorbed species k. It is assumed that the total number of surface active sites is conserved and the saturation sorbent capacity is described by the maximum surface sites density Γ [21]. The uncovered Ni surface is treated as a dummy surface species.

The gaseous adsorption–desorption reactions and surface reactions are written in the general form:

$$\sum_{k=1}^{K_g+K_s} \nu'_k \chi_k \Rightarrow \sum_{k=1}^{K_g+K_s} \nu''_k \chi_k \tag{1}$$

where χ_k is the kth species, ν'_k and ν''_k are the stoichiometric coefficients of the reactants and products, K_g and K_s are the number of gaseous species and surface species, respectively. The net molar production rate $\dot{s}_k$ of a gaseous species or a surface species in a heterogeneous reaction are written as:

$$\dot{s}_k = \sum_{i=1}^{N} (\nu''_{ki} - \nu'_{ki}) k_i \prod_{k=1}^{K_g+K_s} c_k^{\nu'_{ki}} \tag{2}$$

where N is the total number of reactions and c_k is the concentration of the kth species. For all the surface reactions and desorption reactions, the reaction rate constant k_i for the ith reaction is presented

Table 3
Heterogeneous reactions mechanism on the Ni surface.

	Reaction	A^a (cm, mol, s)	n^a	E^a (kJ mol^{-1})
Adsorption				
1f	$O_2 + Ni(s) + Ni(s) \rightarrow O(s) + O(s)$	$1.000 \times 10 - 02^b$	0.0	0.00
2f	$CO_2 + Ni(s) \rightarrow CO_2(s)$	$1.000 \times 10 - 05^b$	0.0	0.00
3f	$CO + Ni(s) \rightarrow CO(s)$	$5.000 \times 10 - 01^b$	0.0	0.00
Desorption				
1b	$O(s) + O(s) \rightarrow Ni(s) + Ni(s) + O_2$	$4.283 \times 10 + 23$	0.0	474.95
2b	$CO_2(s) \rightarrow CO_2 + Ni(s)$	$6.447 \times 10 + 07$	0.0	25.98
3b	$CO(s) \rightarrow CO + Ni(s)$	$3.563 \times 10 + 11$	0.0	111.27
		θCO(s)		−50.00[c]
Surface reactions				
4f	$C(s) + O(s) \rightarrow CO(s) + Ni(s)$	$5.200 \times 10 + 23$	0.0	148.10
4b	$CO(s) + Ni(s) \rightarrow C(s) + O(s)$	$1.354 \times 10 + 22$	−3.0	116.12
		θCO(s)		−50.00[c]
5f	$CO(s) + O(s) \rightarrow CO_2(s) + Ni(s)$	$2.000 \times 10 + 19$	0.0	123.60
		θCO(s)		−50.00[c]
5b	$CO_2(s) + Ni(s) \rightarrow CO(s) + O(s)$	$4.653 \times 10 + 23$	−1.0	89.32

[a] Arrhenius parameters for the rate constants are written in the form: $k = ATn\exp(-E/RT)$.
[b] Sticking coefficient.
[c] Coverage-dependent activation energy.

in the Arrhenius form:

$$k_i = A_i T^{n_i} \exp\left(-\frac{E_i}{RT}\right) \prod_{k=1}^{K_g+K_s} \theta_k^{\mu_{ki}} \exp\left(-\frac{\varepsilon_{ki}\theta_k}{RT}\right) \quad (3)$$

where A_i, n_i and E_i are the pre-exponential factor, temperature exponent and activation energy listed in Table 3, R is the gas constant, T is the temperature,ε_{ki} describes the species coverage-dependency of the rate constant. For most reactions, which are independent of species coverage, ε_{ki} is zero. For reactions 3b, 4b and 5f, the reaction rate constants depend on the CO(s) coverage, $\theta_{CO(s)}$.

For adsorption reactions, the rate constants are expressed in terms of the sticking coefficient form:

$$k_i = \frac{S_i^0}{\Gamma^\gamma}\sqrt{\frac{RT}{2\pi W}} \quad (4)$$

where S_i^0 is the initial sticking coefficient and W is the molecular weight of the gas-phase species. And

$$\gamma = \sum_k^{K_s} \nu'_{ki} \quad (5)$$

Sticking coefficient S_i^0 is temperature dependent and expressed as

$$S_i^0 = a_i T^{b_i} \exp\left(-\frac{d_i}{RT}\right) \quad (6)$$

where a_i and b_i are dimensionless parameters and d_i has the compatible units with RT. These parameters can be treated as Arrhenius number which also listed in Table 3.

For the YSZ surface, few validated reaction mechanisms are available in the literature. Vogler et al. [17] considered molecular adsorption and desorption of water, water dissociation, and bulk-surface exchange. In this study, we neglect CO and CO_2 adsorption and desorption on the YSZ surface, and only consider the bulk-surface exchange of oxygen. Transport of bulk oxygen species takes place by a vacancy diffusion mechanism. The reaction formula and reaction data is given by

$$O^{2-}(YSZ) + (YSZ, bulk) \underset{YSZ,1b}{\overset{k_{YSZ,1f}}{\rightleftarrows}} (YSZ) + O^{2-}(YSZ, bulk) \quad (7)$$

where $k_{YSZ,1f}$ is determined from mass action kinetics, $k_i = k_{i,0}\exp(-(E_i/RT))$ with $k_{i,0} = 1.6$ and $22\,cm^2\,mol^{-1}\,s^{-1}$, and activation energy $E_i = 90{,}900\,J\,mol^{-1}$. $k_{YSZ,1b}$ is determined from the equilibrium constant.

3.2.2. Anode electrochemistry

Theoretical formulation and computational modeling of elementary charge-transfer chemistry have already been suggested from different researchers [22,16,23–25]. Here, the anode electrochemical reactions were taken from the model on the patterned SOFC anode [26] and validated by the polarization curves and EIS experimental results. CO charge transfer pathway is considered in this study:

$$CO(Ni) + O^{2-}(YSZ) \underset{k_{ct,CO,b}}{\overset{k_{ct,CO,f}}{\rightleftarrows}} CO_2(Ni) + (YSZ) + 2e^- \quad (8)$$

where $k_{ct,CO,f}$ and $k_{ct,CO,b}$ are the forward and backward reaction rates CO charge transfer reaction.

According to Faraday's law, the current source at the anode, and depending on the charge transfer step, can be expressed as follows:

$$Q_{an} = i_{0,an} L_{TPB} \quad (9)$$

$$i_{0,an} = 2F(k_{ct,f,CO} c_{O^{2-}(YSZ)} c_{CO(Ni)} - k_{ct,b,CO} c_{(YSZ)} c_{CO_2(Ni)}) \quad (10)$$

where Q_{an} is the volumetric specific Faradic current, F is the Faraday constant, L_{TPB} is TPB length per unit volume. $i_{0,an}$ is the length specific current density. $c_{CO(Ni)}$ and $c_{CO_2(Ni)}$ denote the surface concentrations of CO and CO_2 adsorbed on the Ni surface, respectively. $c_{O^{2-}(YSZ)}$ and $c_{(YSZ)}$ denote volumetric concentrations of oxygen interstitial and oxygen vacancy in the ionic conductor.

The forward and backward charge transfer reaction rates are written as follows:

$$k_{ct,f,i} = k_{ct,f,i}^0 \exp\left(\frac{-(1-\alpha)n_e F}{RT}\eta_{an}\right) \quad (11)$$

$$k_{ct,b,i} = k_{ct,b,i}^0 \exp\left(\frac{\alpha n_e F}{RT}\eta_{an}\right) \quad (12)$$

where α is the charge transfer coefficient. Here, it should be noted that the global representations of charge-transfer chemistry the symmetry factors do not sum to unit. However, to simplify the model parameters, the single charge transfer coefficient was adopted instead of anodic and cathodic symmetry factors. η_{an} is the anodic overpotential, which is defined as:

$$\eta_{an} = V_{elec,an} - V_{ion,an} - V_{ref,an} \quad (13)$$

In this study, the anode reference potential $V_{ref,an}$ was set to zero. The $V_{elec,an}$ is the electronic potential of nickel at the TPB interface and the $V_{ion,an}$ is the ionic potential at the TPB interface. The parameters $k^0_{ct,f,CO}$, $k^0_{ct,b,CO}$ are calculated from:

$$k^0_{ct,f,CO}=\frac{i_{0,CO}}{2FL_{TPB}c^0_{O^{2-}(YSZ)}c^0_{CO(Ni)}},\quad k^0_{ct,b,CO}=\frac{i_{0,CO}}{2FL_{TPB}c^0_{(YSZ)}c^0_{CO_2(Ni)}} \tag{14}$$

where i_0 is the exchange current density, c^0 denotes the species surface concentrations at equilibrium. With volumetric concentrations of oxygen interstitial and oxygen vacancy in the ionic conductor, the equilibrium surface concentration of CO(Ni) and CO_2(Ni) can be determined by making the calculate open circuit voltage agree well the experimental open circuit voltage after iterations.

The exchange current density here can be fitted in Arrhenius form:

$$i_{0,CO} = k_{CO}\exp\left(-\frac{\Delta G_{CO}}{RT}\right) \tag{15}$$

where k and ΔG are the tuning parameters in Arrhenius representation when comparing the simulated polarization curve with the experimental results.

3.2.3. Charge balance

For the electrodes, the charge balance equations can be formulated as

$$\nabla\left(-\sigma^{eff}\nabla V_i\right) = Q \tag{16}$$

where Q is the current source, V_i and V_j are the electric potential of either ionic or electron conductor phases, σ^{eff} is the corresponding conductor phase effective conductivity.

The governing equations for the electrode charge balances are summarized as follows:

- Ionic charge at the cathode:

$$\begin{aligned}\nabla\cdot(-\sigma^{eff}_{ion,ca}\nabla V_{ion,ca}) &= Q_{ion,ca}\\ &= -i_{0,ca}S_{TPB,ca}\left(\frac{c^{TPB}_{O_2}}{c^{bulk}_{O_2}}\exp\left(\frac{\alpha n_e F(V_{elec,ca}-V_{ion,ca}-V_{ref,ca})}{RT}\right)\right.\\ &\quad\left.-\exp\left(-\frac{(1-\alpha)n_eF(V_{elec,ca}-V_{ion,ca}-V_{ref,ca})}{RT}\right)\right)\end{aligned} \tag{17}$$

- Electronic charge at the cathode:

$$\nabla\cdot(-\sigma^{eff}_{elec,ca}\nabla V_{elec,ca}) = Q_{elec,ca} = -Q_{ion,ca} \tag{18}$$

- Ionic charge at the anode:

$$\nabla\cdot(-\sigma^{eff}_{ion,an}\nabla V_{ion,an}) = Q_{ion,an} = Q_{an} \tag{19}$$

- Electronic charge at the anode:

$$\nabla\cdot(-\sigma_{elec,an}\nabla V_{elec,an}) = Q_{elec,an} = -Q_{an} \tag{20}$$

The Q_{an} is the volumetric Faradic current which can be found in Section 3.2.2. $c^{TPB}_{O_2}$ and $c^{bulk}_{O_2}$ are the cathode oxygen concentrations at the TPB and in the bulk, respectively, α is the charge transfer coefficient, n_e is the number of electrons participating in the reaction.

The cathode exchange current density $i_{0,ca}$ is expressed as

$$i_{0,ca} = \frac{\beta RT}{4F}\exp\left(-\frac{E_{ca}}{RT}\right)(p^{O_2}_{ca})^{0.25} \tag{21}$$

where E_{ca} is 130,000 J mol^{-1} and $\beta = 6.17\times10^{11}\ \Omega^{-1}\,m^{-2}$, which indicate the oxygen interface conductivity [27]. η_{ca} is the cathode local overpotential, which is defined as:

$$\eta_{ca} = V_{elec,ca} - V_{ion,ca} - V_{ref,ca} \tag{22}$$

where $V_{ref,ca}$ is the cathode local relative potential difference between the electronic conductors at a reference state. Similar to the cathode local overpotential, the anode local overpotential η_{an} is defined as

$$\eta_{an} = V_{elec,an} - V_{ion,an} - V_{ref,an} \tag{23}$$

By setting anode reference potential $V_{ref,an}$ to zero, the cathode reference potential $V_{ref,ca}$ equals to the actual cell open circuit voltage (OCV) V_{OCV}. Essentially, the SOFC is a concentration cell of O_2 and the OCV can be determined by Nernst equation as [28]:

$$V_{OCV} = \frac{RT}{n_eF}\ln\left(\frac{p^{O_2}_{ca}}{p^{O_2}_{an}}\right) \tag{24}$$

where $p^{O_2}_{ca}$ and $p^{O_2}_{an}$ are the equilibrium oxygen partial pressures in cathode and anode, respectively. $p^{O_2}_{an}$ can be determined by the heterogeneous reactions and the compositions of fuel in anode.

The electrolyte charge balance equation can be briefly expressed as

$$\nabla\cdot\left(-\sigma^{eff}_{ion,electrolyte}\nabla V_{ion,electrolyte}\right) = 0 \tag{25}$$

where $\sigma^{eff}_{ion,electrolyte}$ is the effective ionic conductivity of electrolyte and $V_{ion,electrolyte}$ is the ionic potential in electrolyte.

3.2.4. Mass balance

The mass balance equation in porous electrode can be formulated as [29]:

$$\nabla\left(-D^{eff}_k\nabla c_{k,g}\right) = R_{k,g} \tag{26}$$

where ε is the porosity of electrode, $c_{k,g}$ is the gas molar concentration, $R_{k,g}$ is the mass balance source term of gaseous specie within the porous electrode, and D^{eff}_k is the effective diffusivity of gaseous species k, which can be formulated as

$$D^{eff}_k = \left(\frac{1}{D^{eff}_{k,mole}} + \frac{1}{D^{eff}_{k,Kn}}\right)^{-1} \tag{27}$$

where $D^{eff}_{k,mole}$ and $D^{eff}_{k,Kn}$ are the effective molecular diffusion coefficient and effective Knudsen diffusion coefficient, respectively. For multi-components gases, the effective molecular diffusion coefficient can be calculated as:

$$D^{eff}_{k,mole} = \left[(1-x_k)\Big/\sum_{\substack{j=1\\ j\neq k}}^{n}\frac{x_j}{D^{eff}_{k,j}}\right] \tag{28}$$

where x_k and x_j are the fractions of molar concentrations of gaseous species k and j, and $D^{eff}_{k,j}$ is the effective binary molecular diffusion coefficient. The effective molecular diffusion coefficient of kth gaseous species is restricted to the situation wherein the species k diffuses in a mixture of stagnant and non-transferring species. Considering the porous material property, effective binary molecular diffusion coefficient $D^{eff}_{k,j}$ and effective Knudsen diffusion coefficient $D^{eff}_{k,Kn}$ can be calculated as

$$D^{eff}_{k,j} = \frac{\varepsilon}{\tau}D_{k,j} = \frac{0.00101\varepsilon T^{1.75}((1/M_k)+(1/M_j))^{1/2}}{\tau p\left[V_k^{1/3}+V_j^{1/3}\right]^2} \tag{29}$$

Table 4
Boundary conditions.

Boundary	Ionic charge	Electronic charge	Mass balance
$\partial\Omega_{cc/fuel}$	Insulation	0	$c_{g,an}$ for gaseous species
$\partial\Omega_{an\_sp/cc}$	Insulation	Continuity	Insulation for surface species
$\partial\Omega_{an\_act/an\_sp}$	Continuity	Continuity	Continuity
$\partial\Omega_{electrolyte/an\_act}$	Continuity	Insulation	Insulation
$\partial\Omega_{ca/electrolyte}$	Continuity	Insulation	Insulation
$\partial\Omega_{ca/air}$	Insulation	V_{ca}	$c_{g,ca}$

$$D_{k,\mathrm{Kn}}^{\mathrm{eff}} = \frac{\varepsilon}{\tau} D_{k,\mathrm{Kn}} = \frac{4}{3}\frac{\varepsilon}{\tau}\bar{r}\sqrt{\frac{8RT}{\pi M_k}} \tag{30}$$

where τ is the tortuosity factor, V is the diffusion volume. The value of diffusion volume 18.0 $m^3\ mol^{-1}$ for CO and 26.7 $m^3\ mol^{-1}$ for CO_2. M is the molecular weight, p is the total pressure of gases, and $\bar{r}$ denotes the average pore radius.

In the cathode, the relationship between the mass balance source term and the current source term can be determined by Faraday's law as

$$R_{O_2} = \frac{Q_{\mathrm{elec,ca}}}{4F} \tag{31}$$

The reaction rate of nitrogen is zero and the molar fraction can be determined by

$$x_{N_2} = 1 - x_{O_2} \tag{32}$$

Different from the cathode, the mass balance source terms in the anode are determined by kinetic reaction rates per unit volume of heterogeneous and electrochemical reactions. For both gaseous and surface species in the anode, the source terms $R_{k,g}$ and $R_{k,s}$ can be expressed in the same form:

$$R_k = S^{\mathrm{eff}} \cdot \dot{s}_k = S^{\mathrm{eff}} \sum_{i=1}^{N} \left(\nu''_{ki} - \nu'_{ki}\right) k_i \prod_{k=1}^{K_g+K_s} c_k^{\nu'_{ki}} \tag{33}$$

where S^{eff} is the effective reaction area per unit volume, which equals to S_{Ni} for heterogeneous reactions.

In addition, since the concentrations of oxygen interstitial and oxygen vacancy in ionic conductor are several orders of magnitude larger than the concentrations of gases and surface species, the variation of concentrations of oxygen interstitial and oxygen vacancy is neglected.

3.3. Boundary conditions

According to the operation conditions and model simplifications, the boundary conditions of charge and mass balances partial differential equations are listed as in Table 4.

The boundary conditions "insulation" and "continuity" mean that the partial derivative is zero and the flux is continuous of the variables at the boundary. $c_{g,an}$ and $c_{g,ca}$ in the table are the molar fractions of gaseous species in the anode and cathode. At the interface of anode and anode chamber, the boundary conditions for surface species are "insulation", which is different from gaseous species. That is because there is no surface species out of the anode. The V_{ca} is the cell operation voltage in the calculation.

3.4. Model parameters

From the model development section of charge balance and mass balance equations, the effective reaction area, TPB area and TPB length are needed in the calculation. The parameter S_{TPB} can be formulated by using the particle coordination number in binary random packing of spheres together with percolation theory as [30,31]

$$S_{\mathrm{TPB}} = \pi \sin^2\theta r_{\mathrm{el}}^2 N_{\mathrm{tot}} n_{\mathrm{el}} n_{\mathrm{io}} Z_{\mathrm{el}} Z_{\mathrm{io}} P_{\mathrm{el}} P_{\mathrm{io}} / Z \tag{34}$$

where Z is the mean coordination number, r_{el} is the mean radius of the electronic conductor particle, θ is the contact angle between the electronic and ionic conductors particles, N_{tot} is the total number of particles per unit volume, n_{el} and n_{io} are the fraction number of electronic and ionic conductor particles, Z_{el} and Z_{io} are the coordination numbers of electron and ion conductor particles, and P_{el} and P_{io} are the whole range connection probabilities of the same kind particles. Here S_{TPB} is treated as the contact area of different types of particles. The detailed model description and parameter calculation can be found in the literature [30,32].

Similar to the calculation S_{TPB}, the parameter L_{TPB} (TPB length per unit volume) can be calculated as

$$L_{\mathrm{TPB}} = 2\pi r_{\mathrm{el}} \sin\theta N_{\mathrm{tot}} n_{\mathrm{el}} Z_{\mathrm{el\text{-}io}} P_{\mathrm{el}} P_{\mathrm{io}} \tag{35}$$

The parameter S_{Ni} (effective Ni surface area per unit volume) can be calculated by the total Ni particles surface area subtracting the contact surface area between Ni and YSZ particles and between two Ni particles around the Ni particles per unit volume. Then, the effective Ni surface area per unit volume can be formulated as

$$S_{\mathrm{Ni}} = \pi r_{\mathrm{el}}^2 n_{\mathrm{t}} n_{\mathrm{el}} \left(4 - \sin^2\theta n_{\mathrm{io}} Z_{\mathrm{el}} Z_{\mathrm{io}} / Z - \sin^2\theta n_{\mathrm{el}} Z_{\mathrm{el}} Z_{\mathrm{el}} / Z\right) \tag{36}$$

The pore structure of the anode support layer was characterized using mercury porosimeter. The mean pore diameter, porosity and total pore area were found to be 0.387 μm, 0.335 and $8.54 \times 10^6\ m^2\ m^{-3}$, respectively. To simplify the calculation, the mean particle diameters of the two conductors are assumed to be the same and equal to the mean pore diameter [32]. With this assumption and the expressions of effective reaction areas, the calculated values of S_{TPB} and S_{Ni} in the anode support layer are 2.22×10^5 and $3.97 \times 10^6\ m^2\ m^{-3}$, respectively.

It is very difficult to characterize the pore structures of anode active layer and cathode layer by experiment since they are very thin and hard to be separated from the button cell. We have used image processing software to determine the pore size and porosity of each layer compared to anode support layer from SEM image based on quantitative stereology. It is found that the mean pore size in anode support layer is nearly 1.2 and 1.5 times of that in cathode layer and anode active layer, but the porosities of all three layers are almost the same. Table 5 lists the porosity, mean pore diameter, S_{TPB} and S_{Ni} in each layer.

Then, the material conductivities and some other calculation parameters can be found in Table 6.

3.5. Solution method

The calculations of model were performed using the finite element commercial software COMSOL MULTIPHYSICS®, Version 3.2.

The button cell performance was calculated at a given cell voltage V_{ca}. For 1D SOFC model, the average current density at a given cell voltage was achieved as that in the electrolyte layer. By setting different cell voltages, a complete polarization curve can be generated.

4. Results and discussion

4.1. Model calibration and validation

Since some model parameters cannot be determined directly from experiments or published literature, a calibration process in

Table 5
Pore structure parameters in porous electrode.

Cell layer	Porosity	Mean pore diameter (μm)	S_{TPB} ($m^2\,m^{-3}$)	L_{TPB} ($m\,m^{-3}$)	S_{Ni} ($m^2\,m^{-3}$)
Anode support layer	0.335	0.193	2.22×10^5	2.76×10^7	3.97×10^6
Anode active layer	0.335	0.129	3.33×10^5	6.20×10^7	5.96×10^6
Cathode layer	0.335	0.161	2.66×10^5	3.97×10^7	–

Table 6
Properties and parameters for model calculation.

Property and parameter	Value or expression	Unit
Ionic conductivity (σ_{ion})		
ScSZ	6.92E4 exp(−9681/T)	$S\,m^{-1}$
YSZ	3.34E4 exp(−10300/T)	$S\,m^{-1}$
Electronic conductivity (σ_{elec})		
LSM	4.2E7/T exp(−1150/T)	$S\,m^{-1}$
Ni	3.27E6−1065.3T	$S\,m^{-1}$
Equivalent ionic conductivity of electrolyte layer ($\sigma_{electrolyte}$)	$-3.622E{-}5T^2 + 0.083T - 46.343$[a]	$S\,m^{-1}$
Concentration of oxygen interstitial in the YSZ ($c_{O^{2-}(YSZ)}$)	4.45E4	$mol\,m^{-2}$
Concentration of oxygen interstitial in the YSZ ($c_{(YSZ)}$)	4.65E3	$mol\,m^{-2}$
Maximum surface sites density (Γ)	2.6E−5	$mol\,m^{-2}$
Cathode tortuosity (τ_{ca})	3.0	
Ni felt current collector porosity	0.6[b]	

[a] Experimentally measured.
[b] As received.

a reasonable range to fit the experimental data is necessary. In this paper, the model parameters were tuned according to the experimental polarization curves with fuel F800-2 (40% CO, 60% CO_2) and F800-4 (10% CO, 90% CO_2) cases at 800 °C. The tuning parameter values are listed in Table 7. Once the model parameters are determined, they were not changed in other calculations.

It can be seen that the tortuosity of both the anode and cathode is set at 3 and the tortuosity of the Nickel felt layer is set at 2. It seems reasonable since the observed range for porous sintered ceramics is usually 2–10, and most often in the range of 2–6 [33]. The transfer coefficient α depends on the symmetry of the activation barrier, usually ranges from about 0.3 to 0.6.

Fig. 2 shows the modeling and experimental polarization curves for various CO/CO_2 fuel mixtures at 750/800/850 °C. It can be seen that the modeling polarization curves agree well with the experimental data at 800 °C with composition 10% CO, 90% CO_2 and composition 40% CO, 60% CO_2, which are the base cases for model calibration. It should be noted that there are the distinct kinks around 0.5 V in each polarization curve. However, this phenomenon is not considered in the proposed model. As a preliminary interpretation, this phenomenon may be due to the unstable periodic reaction rate at certain operating voltages which has been suggested by Holtappels et al. [34]. As the CO concentration decreases, the OCV and cell performance decreases significantly. It is clear that there is a limiting current density at zero voltage caused by anodic concentration polarization. The simulated limiting current densities also match well with the values found experimentally. While, it can be found that the curvature of the polarization curves is more significant with the decreasing of CO content due to the concentration effects at lower operating voltage.

Table 7
Model tuning parameters.

Parameters	Value
Cathode tortuosity	3
Cathode electrochemical kinetics parameter, β ($\Omega^{-1}\,m^{-2}$)	1.26×10^9
Cathode charge transfer coefficient (α_{ca})	0.33
Anode tortuosity	3
Anode current collector Ni felt tortuosity	2
Anode charge transfer coefficient (α_{an})	0.6
Anodic electrochemical kinetics parameter, k_{CO} ($A\,m^{-1}$)	1.68E15
Anodic electrochemical kinetics parameter, ΔG_{CO} ($J\,mol^{-1}$)	165615

The polarization curve at 750 and 850 °C has similar features to that at 800 °C. At 750 and 850 °C, the modeling results agree well with the experimental data at low current density but deviate from experimental data for some cases at high current density, which shown in Fig. 2(a) and (c). The modeling results at 750 °C underestimate the diffusion resistance of concentration polarization slightly at high current density. For higher CO content (e.g. >50%) at 750 °C, the concentration polarization is not significant. The calculated limiting current densities are lower than experimental data at 850 °C, which is more pronounced in high CO content cases. The model overestimates the diffusion resistance of concentration polarization, especially at higher current density. The simplification of model geometry might be the important source of the derivation. The anode of button cell is larger than the cathode, which result in the non-uniform distributions of gas concentration in anode in radial direction. In fact, the model is not exactly accorded with 1D geometry assumption and this assumption will lead to the deviation in calculation, especially for the high current cases. Comparison between the modeling results and experimental data in Fig. 2(a)–(c) indicates that the cell performance increases and concentration polarization becomes more significant with the increasing of temperature for the same CO/CO_2 composition. Therefore, the influence of geometry simplification is more obviously at 850 °C, which shown in Fig. 2(c). In addition, the neglect of bulk diffusion in anode chamber also adds contribution to the deviation between the calculated results and experimental data at high current density.

4.2. Species concentration distributions within anode

Since the electrode is very thin and works at high temperature, it is very difficult to characterize the important parameter distribution, especially hard to get the surface reaction elements information. In this section, the elementary surface concentra-

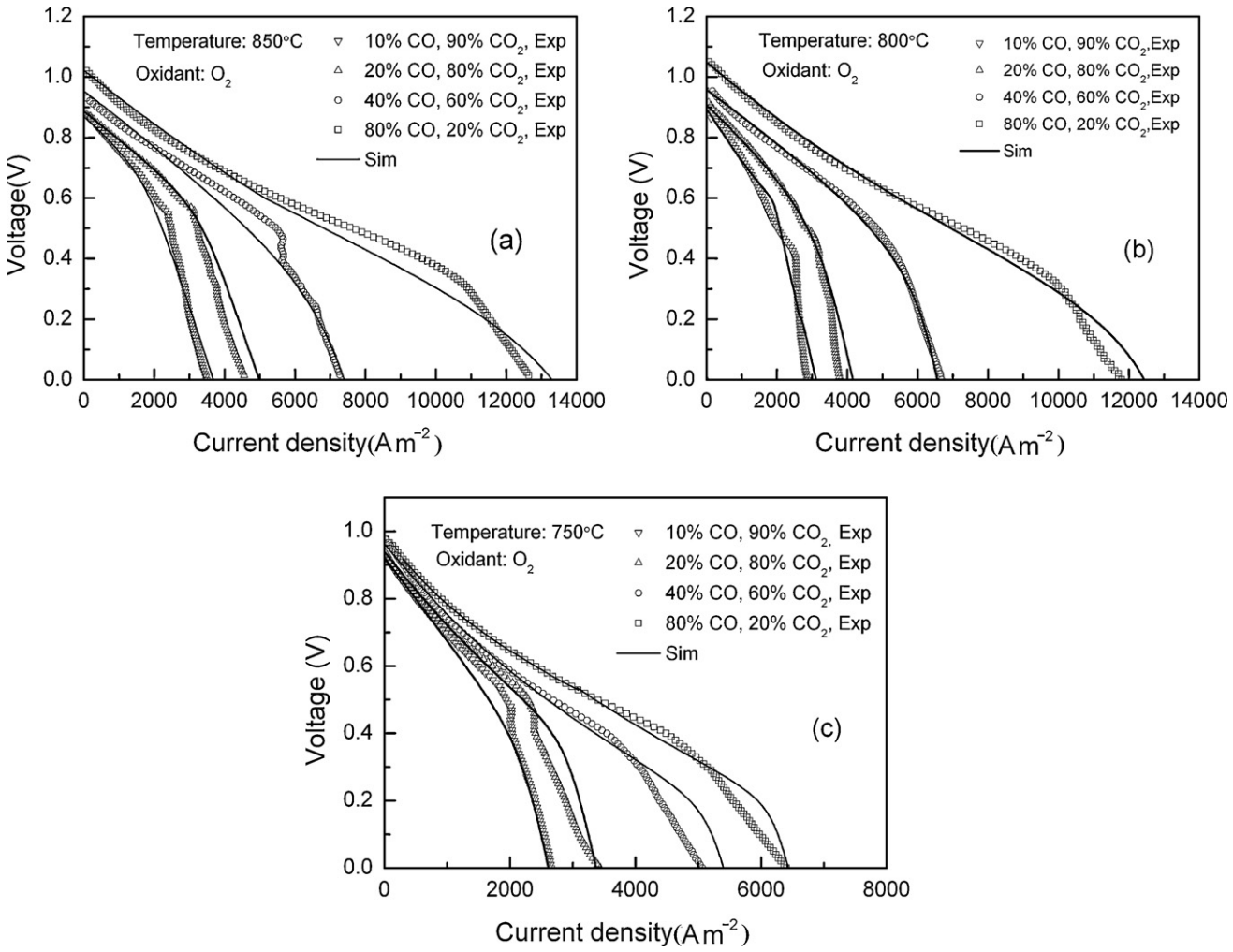

Fig. 2. Modeling and experimental polarization curves for various CO/CO_2 fuel mixtures (a) 850 °C; (b) 800 °C; and (c) 750 °C.

tion indicates the concentration on the Ni surface, which does not include the distributed information of elementary species near the TPB.

Fig. 3 shows the effects of temperature on the surface coverage of NI(s), CO(s), H(s) and O(s) for fuel mixture 80% CO and 20% CO_2 at 800 °C and cell voltage at 0.8 V. It can be seen that the CO(Ni) and (Ni) (Ni vacancies) are the major species in anode, while CO_2(Ni), O(Ni) are the minor species which is at the order of 1e−5 to 1e−6. The surface species turn to equilibrium quickly near the anode outer surface as gases species due to the rapid heterogeneous reactions. The calculation results indicated that the coverage of CO(Ni) and O(Ni) decreases; the coverage of CO_2(Ni) and (Ni) increases with the increasing of the temperature from 750 °C to 850 °C. In addition, it can be found that the CO(Ni) coverage decreases along the electrode thickness direction. In fact, the electrochemical reaction goes fast near the electrode/electrolyte interface and thus consumed more CO(Ni) surface species to react with oxygen ions.

Fig. 4 shows the coverage distribution of various surface species in the anode for fuel mixture 80% CO and 20% CO_2 at 800 °C and cell voltage at 1.0, 0.8 and 0.6 V. The calculation results indicated that variation of the surface species distribution along the electrode became more significant at lower operating voltage due to the relatively faster electrochemical reaction rates. Especially when the cell voltage is kept at 0.6 V, the coverage ratio of the surface species changes rapidly. This indicated that the species surface concentration is much larger at high operating mode compared with that at low overpotential operating mode, which may also lead to the surface diffusion phenomenon at local catalyst surface.

Fig. 5 further shows the effects of fuel compositions on the surface coverage of (Ni), CO(Ni), O(Ni) and CO_2(Ni) with operating temperature at 800 °C and cell voltage at 0.8 V. It can be seen that the surface species coverage is significantly affected by the fuel composition. When CO content increases from 20% to 80%, the CO(Ni) surface coverage get larger, while the (Ni), CO_2(Ni) and O(Ni) contents get smaller.

4.3. Modeling analysis on carbon deposition phenomenon

The effects of carbon deposition process will be discussed in both experimental and modeling aspects in this section. However, it should be noted that in the model, only the carbon coverage on the catalyst surface is considered, while the phenomenon of deposited carbon growth on the anode surface is not considered. Thus, the modeling analysis is focused on the qualitative or semi-qualitative but not quantitative. In addition, since it is hard to detect the carbon deposition process directly from experiments, the modeling analysis will be significant important for operating strategy choice and for understanding the detailed electro-thermal chemistry with SOFC anode.

The effect of temperature on carbon deposition degree is shown in Table 8. It suggests that the carbon atomic percentage decreases with the temperature. Then, the modeling results of carbon cov-

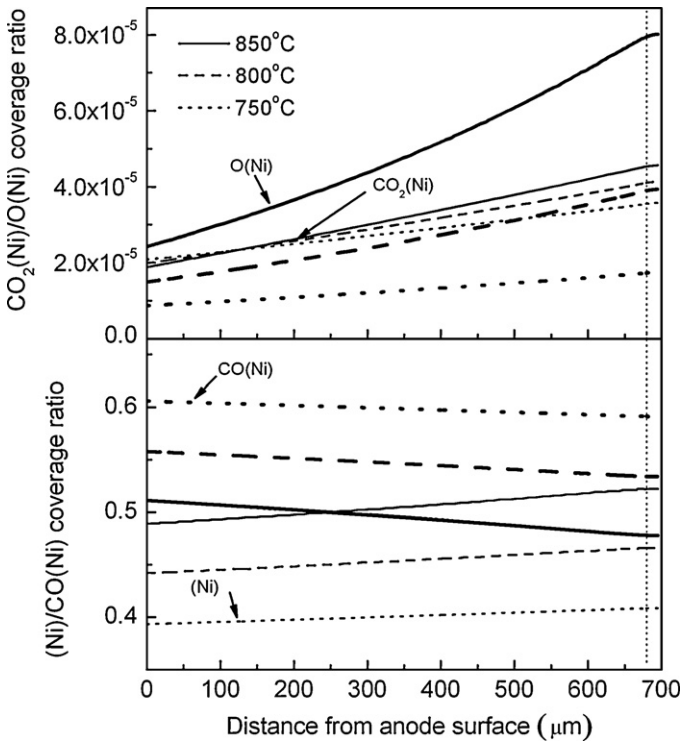

Fig. 3. Coverage distributions of surface species within anode at 750/800/850 °C.

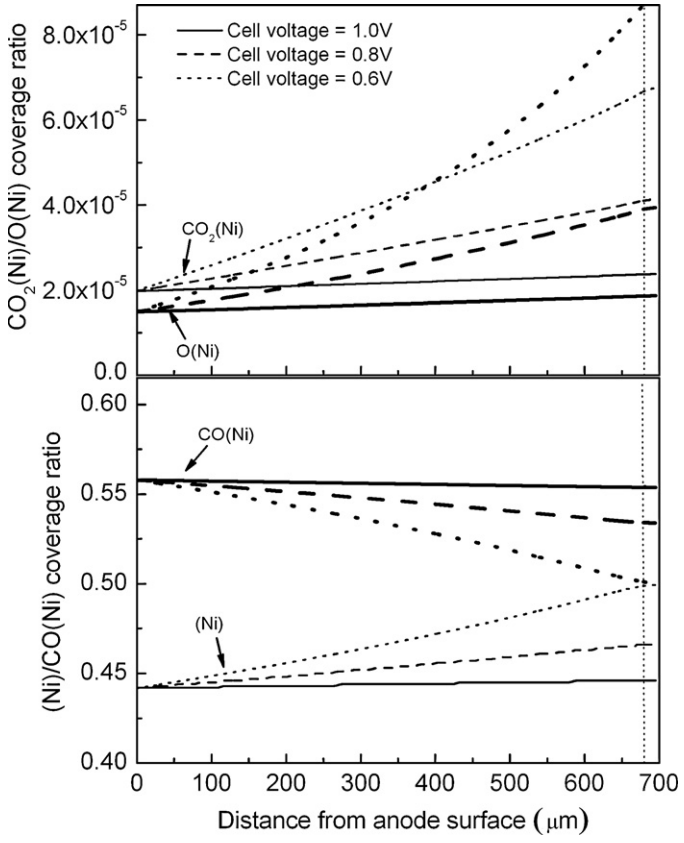

Fig. 4. Coverage distributions of surface species within anode at different operating voltages (1.0 V/0.8 V/0.6 V).

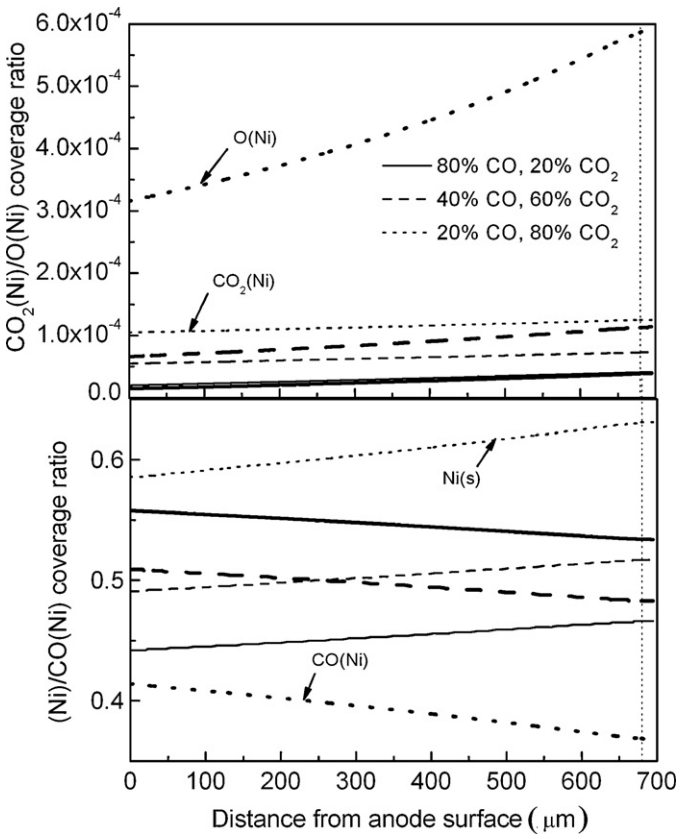

Fig. 5. Coverage distributions of surface species within anode with different fuel compositions.

Table 8
Effects of temperature on anode carbon deposition degree.

Temperature (°C)	Atomic percentage (at.%) within anode				
	C	O	Ni	Zr	Y
750	12.87	56.56	11.71	16.54	2.32
800	11.60	58.18	11.62	16.38	2.22
850	10.72	57.52	13.30	16.39	2.07

erage variation at different temperatures are shown in Fig. 6. The modeling results also indicate that the surface coverage of C(Ni) increases significantly when the temperature deceases at certain current density, which is a good qualitative agreement with the experimental results. And, it also suggests that the carbon deposition is mitigated at higher current density. In fact, at a higher current density, more surface specie O(s) is generated in electrochemical reactions and hence reducing the possibility of carbon deposition on Ni surfaces. Thus, it can be deduced that the carbon deposition degree of syngas fueled SOFC could be reduced by raising the operation temperature and reducing cell voltage.

The effects of fuel composition on carbon deposition degree at 750 °C are shown in Table 9. It suggests that the carbon atomic per-

Table 9
Effects of CO mole fraction in the fuel on the anode carbon deposition degree.

CO mole fraction (%)	Atomic percentage (at.%) within anode				
	C	O	Ni	Zr	Y
90	14.32	54.18	12.78	16.60	2.13
50	12.82	58.15	10.28	16.55	2.21
10	10.77	56.29	12.18	18.26	2.51

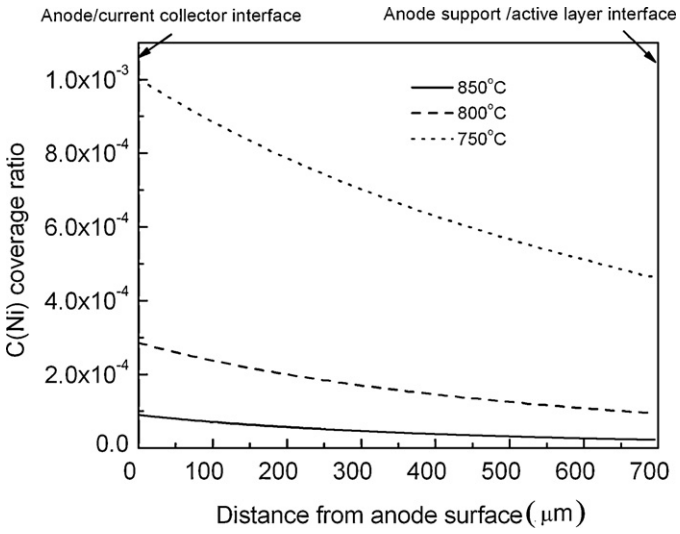

Fig. 6. Surface carbon species converge within anode at 750/800/850 °C.

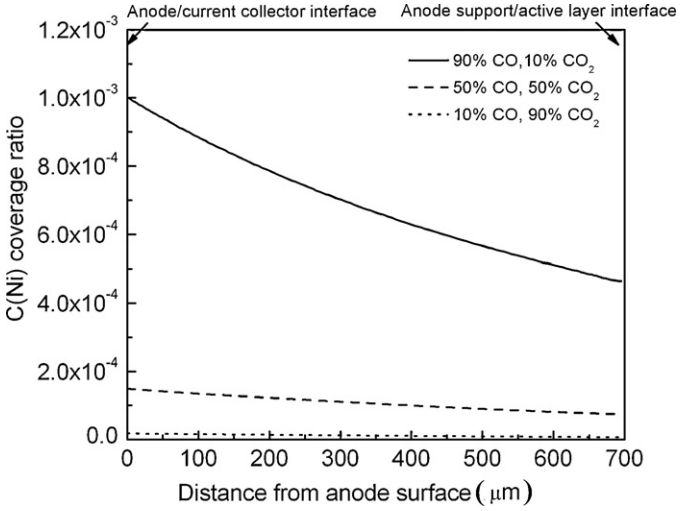

Fig. 7. Surface carbon species converge within anode at different CO contents.

centage increases with the mole fraction of CO in the fuel. Fig. 7 further shows the modeling results of fuel composition effects on carbon deposition degree. It suggests that the degree of carbon deposition aggravates as the CO content decreases. This qualitative trend agreed well with the experimental observations. It also indicated that when the CO mole fraction is less than 50%, the C(Ni) coverage ratio can be kept at the level under 1.5e−4. However, when the CO mole fraction increased to 90%, the C(Ni) coverage ratio increases fast to 1e−3 level, which is almost 6 times larger than that at 50% CO fuel composition. It further indicated the necessity for keeping the CO content at a lower level to release the carbon deposition risk.

5. Conclusion

A detailed one-dimension elementary reaction model of an anode-supported SOFC operating with CO/CO_2 mixtures based on button cell geometry was developed. The model incorporated anodic elementary heterogeneous reactions, electrochemical kinetics, electrodes microstructure and complex transport phenomena (mass and charge transport) within electrode.

The model was calibrated and validated with the experimental data with different CO and CO compositions at 750, 800 and 850 °C. The results indicated that the model agreed reasonably well with the experimental data. The model can well be applied for the detailed understanding of the electro-thermal chemical and transport processes with porous electrode and on electrode particles surface, and also the model can be used in the cell operating condition optimization.

For the heterogeneous reactions, CO(Ni) and Ni vacancies are the major species in anode, while C(Ni), CO_2(Ni) and O(Ni) are the minor species with the coverage is about 10^{-5} to 10^{-6}. As the cell voltage decreases, the faster electrochemical reactions resulting in the increasing of CO_2(Ni)and O(Ni) and the decreasing of CO(Ni), C(Ni). The effects became more obvious near the TPB. The coverage of CO(s) and O(s) decreases with increasing temperature due to the higher desorption rates. In addition, both of the modeling and experimental results indicate that lower temperature and operation voltage are helpful to reduce the possibility of carbon deposition on Ni surfaces. While, as the CO_2 content in the fuel increases, the degree of carbon deposition aggravates.

Acknowledgements

The supports from Projects 20776078 (National Natural Science Foundation of China, NSFC) and Project 2007AA05Z151 (National High Technology Research and Development Program, 863) are highly appreciated.

References

[1] Y. Matsuzaki, I. Yasuda, J. Electrochem. Soc. 147 (5) (2000) 1630–1635.
[2] K. Eguchi, H. Kojo, T. Takeguchi, et al., Solid State Ionics 152–153 (2002) 411–416.
[3] K. Sasaki, Y. Hori, R. Kikuchi, et al., J. Electrochem. Soc. 149 (3) (2002) A227–A233.
[4] Y. Jiang, A.V. Virkar, J. Electrochem. Soc. 150 (2003) A942–A951.
[5] j. Mizusaki, et al., Solid State Ionics 53–56 (1992) 126–134.
[6] G.O. Lauvstad, R. Tunold, S. Sunde, J. Electrochem. Soc. 149 (12) (2002) E497–E505.
[7] V. Yurkiv, D. Starukhin, H.-R. Volpp, et al., J. Electrochem. Soc. 158 (2011) B5–B10.
[8] C.J. Moyer, N.P. Sullivan, H. Zhu, et al., J. Electrochem. Soc. 158 (2011) B117–B131.
[9] A. Bieberle, L.J. Gauckler, Solid State Ionics 146 (2002) 23–41.
[10] A. Bieberle, The electrochemistry of solid oxide fuel cell anodes: experiments, modeling, and simulation, Ph.D. Dissertation, 2000, Swiss Federal Institute of Technolgoy, Zurich.
[11] M. Mogensen, T. Lindegaard, Proceedings of the 3rd Int. Symp. on Solid Oxide Fuel Cells, Honolulu, HI, 1993, pp. 484–493.
[12] B. De-Boer, SOFC anode: hydrogen oxidation at porous nickel and nickel/YSZ cermet electrodes, Ph.D. Dissertation, 1998, Universiteit Twente, Netherland.
[13] J. Mizusaki, J. Electrochem. Soc. 141 (8) (1994) 2129–2134.
[14] S.P. Jiang, S.P.S. Badwal, J. Electrochem. Soc. 144 (1997) 3777–3784.
[15] P. Holtappels, L.G.J. de Haart, U. Stimming, J. Electrochem. Soc. 146 (5) (1999) 1620–1625.
[16] W.G. Bessler, J. Warnatz, D.G. Goodwin, Solid State Ionics 177 (2007) 3371–3383.
[17] M. Vogler, A. Bieberle, L. Gauckler, et al., J. Electrochem. Soc. 156 (5) (2009) B663–B672.
[18] E.S. Hecht, G.K. Gupta, H. Zhu, A.M. Dean, R.J. Kee, L. Maier, O. Deutschmann, Appl. Catal. A 295 (2005) 40–51.
[19] V.M. Janardhanan, O. Deutschmann, J. Power Sources 162 (2006) 1192–1202.
[20] H. Zhu, R.J. Kee, J. Electrochem. Soc. 153 (2006) A1765–A1772.
[21] R.J. Kee, M.E. Coltrin, P. Blarborg, Chemically Reacting Flow, John Wiley & Sons Inc., Hoboken, NJ, 2003.
[22] W.G. Bessler, S. Gewies, M. Vogler, Electrochim. Acta 53 (2007) 1782–1800.
[23] H. Zhu, R.J. Kee, V.M. Janardhanan, O. Deutschmann, D.G. Goodwin, J. Electrochem. Soc. 152 (2005) A2427–A2440.
[24] H. Zhu, R.J. Kee, J. Electrochem. Soc. 155 (2008) B715–B729.
[25] D.G. Goodwin, H. Zhu, A.M. Colclasure, et al., J. Electrochem. Soc. 156 (2009) B1004–B1021.
[26] Y. Shi, W. Lee, A. Ghoniem, Proceedings of the ASME 2010 Eighth International Fuel Cell Science, Engineering and Technology Conference, June 14–16, Brooklyn, NY, USA, 2010, FuelCell2010-33205.
[27] S. Nagata, A. Momma, T. Kato, Y. Kasuga, J. Power Sources 101 (2001) 60–71.
[28] R.P. O'Hayre, S.W. Cha, W. Colella, F.B. Prinz, Fuel Cell Fundamentals, John Wiley & Sons Inc., Hoboken, NJ, 2006.

[29] R. Suwanwarangkul, E. Croiset, M.W. Fowler, P.L. Douglas, E. Entchev, M.A. Douglas, J. Power Sources 122 (2003) 9–18.
[30] P. Costamagna, P. Costa, V. Antonucci, Electrochim. Acta 43 (1998) 375–394.
[31] S.H. Chan, Z.T. Xia, J. Electrochem. Soc. 148 (2001) A388–A394.
[32] J. Divisek, R. Wilkenhoner, Y. Volfkovich, J. Appl. Electrochem. 29 (1999) 153–163.
[33] R.E. Williford, L.A. Chick, G.D. Maupin, et al., J. Electrochem. Soc. 150 (2003) A1067–A1072.
[34] P. Holtappels, L.G. Haart, U. Stimming, et al., J. Appl. Electrochem. 29 (1999) 561–568.